Title:	**PROTON RADIOGRAPHY FOR AN ADVANCED HYDROTEST FACILITY**
Author(s):	Christopher L. Morris
Submitted to:	
	http://lib-www.lanl.gov/la-pubs/00357005.pdf

PROTON RADIOGRAPHY FOR AN ADVANCED HYDROTEST FACILITY

Christopher L. Morris (for the PRAD Collaboration)
Los Alamos National Laboratory
P-25, MS H846
Los Alamos, NM 87545
(505) 667-5652

ABSTRACT

Analysis of data from BNL experiment 933 is presented. Results demonstrate that proton radiography can meet many of the requirements for an Advanced Hydrotest Facility (AHF). Results for background, position resolution, metrology, quantitative radiography, material identification, and edge resolution are presented.

INTRODUCTION

In transmission radiography, the transmitted flux through an object is used to measure its areal density. The transmission, t_l is given in terms of the path length l through the object and mean free path l by:

$$t_l = e^{-l/l} \ . \qquad (1)$$

This is measured as a function of position and inverted to calculate the thickness of the object as:

$$l = -l \ln\left(t_l\right). \qquad (2)$$

Here, l is given by:

$$l = \frac{1}{rs} \ . \qquad (3)$$

A simple model for proton radiography can been obtained by assuming the nuclear scattering results in the removal of beam particles from the transmitted flux described by Eq. (1) and that Coulomb scattering can approximated by assuming transmitted particles are scattered into a Gaussian shaped angular distribution. In this approxima tion integration of the angular distribution between limits imposed by angle collimators at the Fourier points in the lenses[1] results in closed form expressions for the transmission. A beam transmitted though an object acquires an angular spread,

$$I(q) = \frac{1}{pq_0} e^{\left(-q^2/2q_0^2\right)}, \qquad (4)$$

where

$$q_0 = \frac{14.1}{pb} \sum_i \frac{r_{Ai}}{X_i} \ . \qquad (5)$$

Here p is the beam momentum, $b = v/c$ where v is the beam velocity and c is the speed of light; X_i is the radiation length for the $i'th$ material. Throughout the rest of this work the sum will be implied. This can be integrated between angular limits, q_1 and q_2,

$$I(q)\sin(q)dqdf = e^{-\left(X_2/r_x\right)} - e^{-\left(X_1/r_x\right)}, \qquad (6)$$

where $r_x = \sum_i (r_{Ai}/X_i)$ is the areal density of an object, $X_1 = p^2 q_1^2 /(2 \times 14.1^2)$, with a characteristic areal density associated with the large polar angle limit, q_1, and, $X_1 = p^2 q_2^2 /(2 \times 14.1^2)$, with a characteristic areal density associated with the small polar angle limit, q_2.

Multiple lenses on a single axis, with different angular collimators, allow Coulomb radiation lengths to be separated from nuclear attenuation lengths in proton radiography. Transmission through a single lens, including both nuclear and Coulomb attenuation, is given by

$$I = e^{-r_l}\left(e^{-\left(X_2/r_x\right)} - e^{-\left(X_1/r_x\right)}\right). \qquad (7)$$

The most precision can be obtained with a set of two lenses where the first is optimized to measure only nuclear attenuation by having a large aperture. If the small angle cut is zero and the large angle limit is large enough so that second term can be ignored transmission through the first lens in a two-lens system is

$$I_1 = e^{-r_1} .$$ (8)

If the second lens has a large, large angle limit, but does have a small angle cut (Ferm collimator[2]) than transmission through the second lens is given by

$$I_2 = e^{-r_1 - (x_2/r_x)} .$$ (9)

Equations (5) and (6) can be solved for the nuclear attenuation length weighted areal densities,

$$r_1 = \ln(I_1) ,$$ (10)

and the radiation-length weighted areal densities,

$$\frac{r_x}{X_2} = \frac{1}{\ln(I_1) - \ln(I_2)} .$$ (11)

In this report we present data from experiment 933, recently completed at Brookhaven National Laboratory, which demonstrate many of the features of proton radiography. A matching section and two lenses were constructed using existing refurbished 8Q48 quadrupole magnets in line U at the AGS. This system was installed and commissioned using single pulses of up 10^{11} protons at 24 GeV/c provided by the alternating gradient synchrotron (AGS). The pulse intensity was administratively limited to this value by AGS safety requirements. A picture looking upstream from the end of the second lens is shown in Fig. 1.

BEAM CHARACTERIZATION

Diagnostic data were obtained on a pulse by pulse basis with transformers, which measured proton fluxes at three locations in the beam line; upstream of the diffuser location, and at each of the down image locations downstream. The beam position and angle at the diffuser location were monitored using two CCD cameras looking at two phosphors, one mounted on the diffuser and one located approximately 6 m upstream of the diffuser. Combining the data from these measurements in principle allows accurate pixel-to-pixel normalization of transmitted flux trough an object to be obtained by normalizing to the measured fluxes and correcting the beam profile for shifts

in position measured using the upstream images. Although preliminary analysis of the upstream data shows a correlation with the downstream beam spot location[3], this information was not used in the remaining analysis. Since a similar system would have a large impact on AHF costs by removing much of the need for an upstream lens in the matching region, more work on this problem is needed.

The matching lens was tuned by removing the downstream collimator and installing a phosphor and CCD camera system at the collimator location. The beam was centered on the phosphor by steering it at the diffuser location and the spot was minimized by adjusting the matching quadrupoles. One of the matching magnet power supplies was run near the top of its range. The size of the beam at the collimator location corresponded to about 0.5 mrad of angle resolution at the object location. This size, which is related to the emittance of the accelerator, puts a scale on the thinnest objects that can be radiographed. The 0.5 mrad-measured resolution corresponds to about 0.85 radiation lengths or about 6 mm of tungsten. This is radiographically equivalent to having a uniform fixed amount of material in addition to any other object that is in the beam. A diffuse halo amounting to about 4% of the total beam intensity was observed. Beam pictures and lineouts at the collimator location are shown in Fig. 2. The beam emittance can be accounted for radiographically by including it in the transmission.

BACKGROUND MEASUREMENTS

After tuning both the matching magnets and the lens focal length, a 1-mrad collimator was installed in the upstream lens, a 1-cm diameter, 15-cm-long tungsten rod was mounted at the object location at the beginning of the first lens, and images were made with and without the FTO mounted in the object location of the second lens. The tungsten rod produces in a hole in the beam downstream of the fist lens. The background produced by each of the collimators was measured by studying how much this is filled in when an object is put in the beam with the collimator mounted in the downstream lens. The backgrounds measured from the 4.4 and 3 mrad normal and 3 mrad Ferm collimators were 2.1, 3.9, and 4.6% at the limb of the FTO, respectively. Although these are somewhat higher than simulations predict, they are low enough to be easily dealt with. Some of these results are displayed in Fig. 3.

POSITION RESOLUTION AND METROLOGY

Position resolution and accurate metrology are important parameters for AHF applications of proton radiography. Quantitative measures of both of these

parameters were obtained during experiment 933. A more complete description of some the test objects used during experiment 933 can be found in Ref. 4.

The magnetic optics in the beam line and the photon optics in the detectors potentially introduce geometric distortions. These can be measured using a fiducial grid plate, shown in Fig. 4. The fiducial plate places a uniform grid of features across the entire field of view. In the acquired data, the positions of these features can be used to measure geometric distortions.

A radiograph of this object is shown in Fig. 5. The expected structure is clearly visible. The data have been divided by a beam image, and the position scale was offset and adjusted with a rotation and linear scaling in both x and y. The residuals for all of the intersections are plotted in the figure. Some evidence for geometric aberrations can be seen in the residual plots. The rms position error average across the entire field of view is less than 100 mm, with the largest contribution coming from the corners, where geometric aberrations are the largest.

Position resolution was measured using a resolution pattern machined into a 2.5-mm-thick piece of platinum, in both image planes. These data are shown in Fig. 6. The position resolution was measured to be 250 mm FWHM in the first image plane. A similar value was obtained in thicker classified test objects.

STEP WEDGE MEASUREMENTS

After completing the lens characterization, a set of step wedge measurements were completed on tungsten, copper, carbon, and lucite, in order to provide cross sections to be used in quantitative analysis of other test objects. The finite acceptance of the beamline as a function of energy loss and scattering angle in an object can be expressed as an effective cross section, which must be known to reconstruct the density of an object from its radiograph. A simple way to measure the effective cross sections over the range of interest is to use a set of step wedges constructed from the same materials as the object and that span the thickness range of the object.

Figure 7 illustrates the step wedges used in experiment 933. This design using two wedges back to back allows us to make a new configuration, a pair of wedges with small steps separated by a spacer block of the same material. This allows us to make the measurement on steps that differ by a small amount across a large range of total thickness, using only one pair of wedges. The approximate mid-plane symmetry simplifies alignment along the beam direction, and arranging the thickest part of

the wedge to be in the center of the beam provides a better match of attenuation to the flux, optimizing the statistical precision of the cross section measurement for a given proton flux. Detailed descriptions of the actual step wedges used can be found in Ref. 1.

The steps in the analysis of the step wedge data were to first align and average each of the four images plates exposed in each image plane for each picture. Four image plates were used to increase the DQE. Estimates made by comparing actual images with simulations suggested the resulting DQE was in the range of 20–40%. The data from image location one (I1) were divided by a smoothed beam image. The results were "flattened" by fitting a two-dimensional polynomial to the regions of the picture where there was no material in the beam and then dividing the image by this polynomial. This helps to remove artifacts due to beam motion and non-uniform response of the image plates. The data from image location 2 (I2) were taken with a Ferm collimator. These data were rotated to account for the inversion of the lens, aligned with the images from image location 1 (I1), and the divided by the I1 results. The procedure for IL1 is illustrated in Fig. 8.

Cross sections were measured in steps of 1% of an attenuation length up to the full thickness of the FTO for each of the materials. Some of the results for the 10% step wedge are shown in Fig. 9. The fit demonstrates the quality of quantitative agreement obtained between a semi-empirical model and the data. Step wedge data were also taken looking through an additional 345 gm/cm^2 of tungsten. These data illustrate the capability of proton radiography to obtain quantitative data over an extremely wide dynamic range of object thickness. The full set of data for I1 for the tungsten step wedge is shown in Fig. 10.

The data in Fig. 9 demonstrate the potential for material identification. The step wedges have been designed to cover a similar thickness range in nuclear attenuation lengths, but have a much different thickness in Coulomb radiation lengths, with the tungsten being much thicker than the carbon in radiation length units. This results in much more multiple scattering in the tungsten than in the carbon. Because of this there is a dramatic difference in the I2 images, where the tungsten step wedge is clearly visible and the carbon is difficult to discern.

For thin objects Eqs. (10) and (11) apply. This can be seen below where the functions of the transmission given by Eqs. (10) and (11) are plotted for the various 10% step wedges. The slope of these curves, which should be a measure of material type, can be seen to display the expected material dependence.

The tungsten step wedge data span a wide range of thickness. A fit to the entire data set, assuming a Gaussian multiple scattering angular distribution and a Gaussian beam emittance is shown as the solid line in the figure. The function form fitted to the flattened transmission is

$$I = e^{-r_l} \left[\frac{\left(1 - e^{-(X_1/r_x + r_{fixed})}\right)}{\left(1 - e^{-(X_1/r_{fixed})}\right)} \right]. \qquad (12)$$

The offset, r_{fixed}, has been added to account for the finite beam emittance. The denominator has been added to account for the flattening which forces the transmission to be one of zero thickness, even though there is some attenuation due to the beam emittance. This function can be seen to give a good account of the data over a very wide range in step wedge thickness. The fixed offset is also the reason for the nonzero intercept of the curves in Fig. 11.

The approximations in Eq. (12) do not work well for low-Z thin objects because of the long tails on the beam that can be observed in Fig. 2. This can also been seen by the departure from linearity for thin objects in Fig. 11. The small amount of multiple scattering introduced by the low-Z step wedges results in exaggerated attenuation when it is convoluted with the tails on the beam distribution. Nevertheless the materials in the step wedges are clearly distinguished by different slopes. The effect of the angle cut in the first lens leads to the departure from linearity for the thicker steps of tungsten step wedge for which the multiple scattering cone does not fit within the lens acceptance.

QUANTITATIVE DENSITY ANALYSIS

The tungsten densities from the FTO have been reconstructed by using the data analysis procedures similar to those outlined in the step wedge analysis. After the four image plates were averaged, the results were divided by model radiographs of the outer foam and copper shells and then the flattening procedure was applied to the region of the radiograph outside of the tungsten region. The resulting transmission image was transformed from transmission to areal density using the same procedure as was used in the step wedge analysis but being careful to take into account the overlying material, including the outer copper and foam shells of the FTO. The resultant areal density image was centered and volume densities were calculated using a conditioned Abel inversion method described previously.[5]

The resultant volume densities can be compared with the measured tungsten density of $18.28 \pm .07$ gm/cm^3. A histogram of the densities measured on (169 mm)^3 voxels

in the region of the tungsten is shown in Fig. 13. The agreement between radiographic density, and that obtained from metrology is robust and precise at the level of a percent or so. The AHF goal, driven by the criticality requirement, is to measure densities to 1–2% in absolute precision. This result meets that goal for the simple geometry of the FTO.

EDGE RESOLUTION

The half-density contour for both the inner edge and the outer edge of the FTO has been extracted and analyzed to determine the precision with which edges can be extracted from high-energy proton radiography. The AHF requirement for this quantity is 75 mm. The radius for each of the x-y pairs was extracted from the contours, and then the mean and standard deviation of these was calculated. There was no constraint on the radius of curvature and no additional smoothing beyond that from the conditioned-Abel inversion. This analysis provides an unbiased estimate of the precision with which radii can be extracted. Limits to the precision are due to the statistical accuracy of the reconstruction (the exposure of 10^{10} protons) and by systematic sources of error such as magnetic aberrations. The contours are displayed as the red lines in Fig. 14.

The difference between the radii of the extracted contour and the average radius are plotted as a function of x in Fig. 15 for both the inner radius and the outer radius. Also shown in the figure are the mean and the standard deviations averaged over the entire contour.

The average values for the measured outer and inner radii of 4.494 and 1.014 agree well with the known dimensions of the object of 4.500 and 1.000 cm, respectively. However, systematic discrepancies clearly dominate the residuals. This can be seen in Fig. 15 as the large correlation between the residual and x position. The random fluctuations, which are a measure of the statistical uncertainty and which impose the ultimate limit to the precision of edge determination, contribute about 30 mm to the total RMS.

TEST OBJECT MEASUREMENTS

Following this sequence of lens setup and radiographic calibration experiments data were taken on a wide range of test objects. Some of these experiments allowed direct comparisons with DARHT, FXR and microtron x-radiography measurements. The dynamic range and sensitive of flash proton radiography were demonstrated to exceed both the current state of either flash or fixed target x-radiography in the qualitative results of all of these experiments.

CONCLUSIONS

Some strong conclusions can be drawn from the current analysis of data. The quality of radiography necessary to meet or nearly meet the AHF goals for position resolution, density precision, timing, and sensitivity to small density changes have been demonstrated with protons. Concerns about background and dynamic range should be laid to rest. Material identification has been demonstrated. The ability to measure the size and amplitude of the incident beam has been demonstrated. Active cameras operating at DQEs in the tens of percent have been demonstrated.

REFERENCES

1. King NSP, Ables E, Adams K, Alrick KR, Amann JF, Balzar S, Barnes PD, Crow ML, Cushing SB, Eddleman JC, Fife TT, Flores P, " An 800-MeV proton radiography facility for dynamic experiments," *NUCLEAR INSTRUMENTS & METHODS IN PHYSICS RESEARCH SECTION A-ACCELERATORS SPECTROMETERS DETECTORS AND ASSOCIATED EQUIPMENT , v. 424(#1) pp. 84-91 MAR 11, 1999.*

2. C. L. Morris, Eric Ferm, Nick King, Mary Hockaday, Gary Hogan, Kevin Morley, Alexander Saunders, and John Zumbro, "A comparison of collimators and anti-collimators for multiple scattering radiography", LA-UR 00-2934, 2000.

3. Ed Hartouni, talk presented at an E933 collaboration meeting.

4. Peter Barnes, "Test Objects for Calibrating the FTO as part of BNL E933," distributed to the collaboration, 1999.

5. C. Morris, presented in numerous talks and lectures but never well documented.
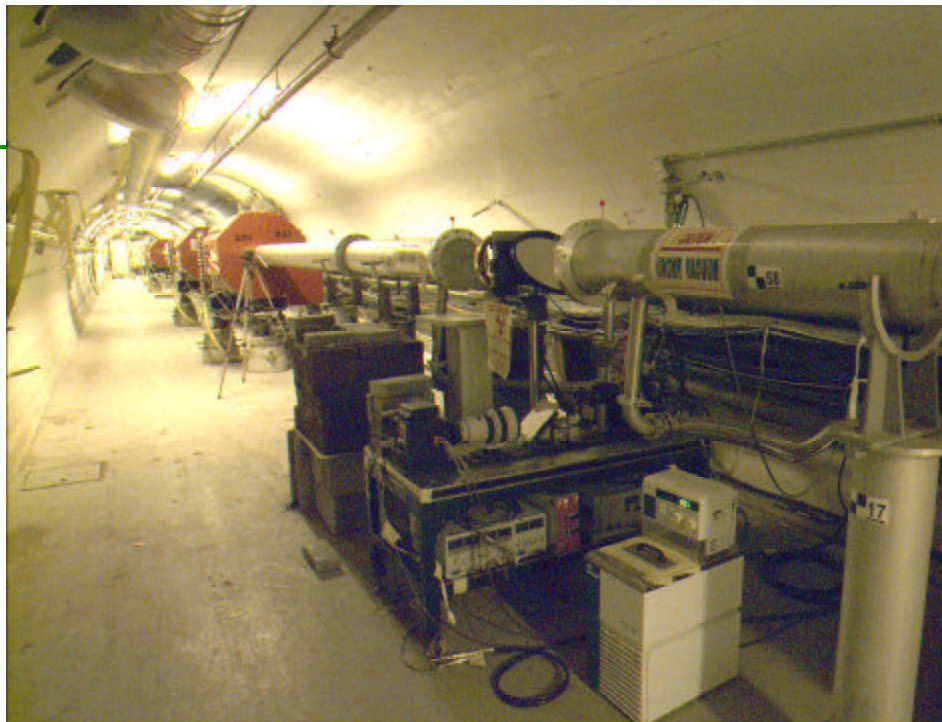
FIGURES

Fig. 1. A view of the experiment 933 setup looking upstream from the first camera location. The active cameras can be seen in the middle of the photograph.

Beam

FTO

Intensity (arb)

run 7018
run 7000

FTO

Beam

x (cm)

- Tails on the beam lead to the apparent background with the Ferm collimator.
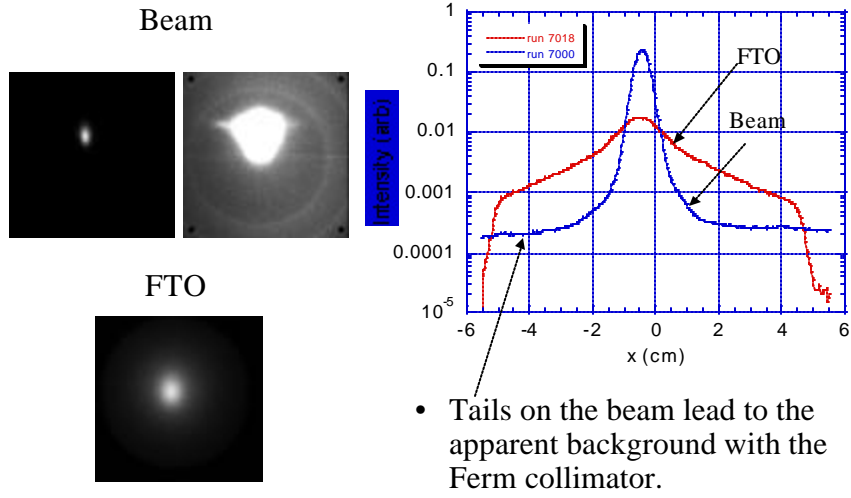
Fig. 2. Images of the beam taken at the collimator location are shown on the left. The top two images are taken with nothing in the beam and the low image is with the FTO in the beam. Lineouts are displayed on the right. The right beam image is displayed with an expanded z scale to show the tail on the beam.
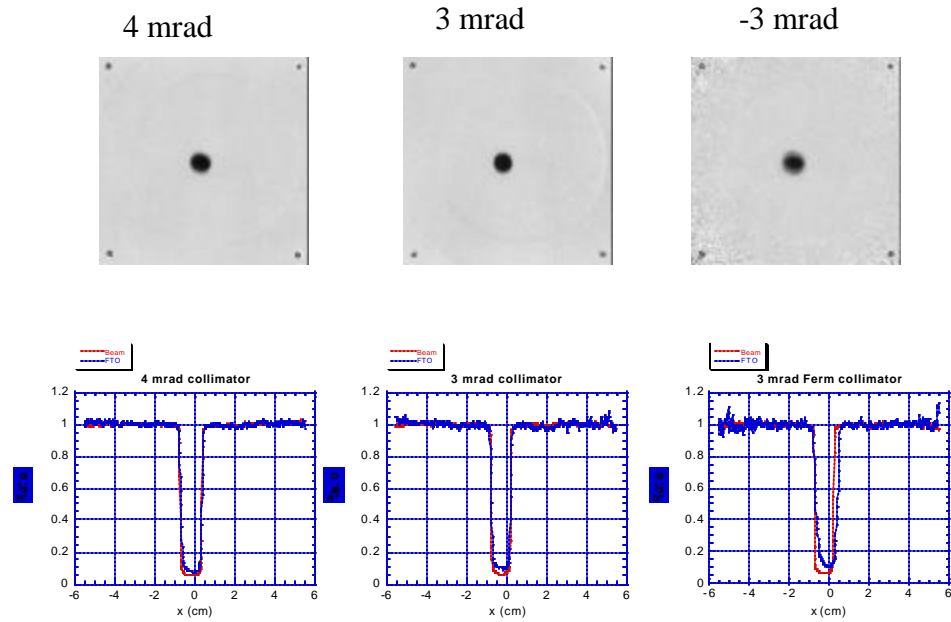
4 mrad   **3 mrad**   **-3 mrad**

Beam
FTO

4 mrad collimator

x (cm)

Beam
FTO

3 mrad collimator

x (cm)

Beam
FTO

3 mrad Ferm collimator

x (cm)

Fig. 3. Top: Ratios of radiographs of the FTO with the shadow bar in to the shadow bar out for each of the collimators. Bottom: Lineouts of the beam ratioed images with the shadow bar in and the FTO-in in blue and with the FTO-out in red.
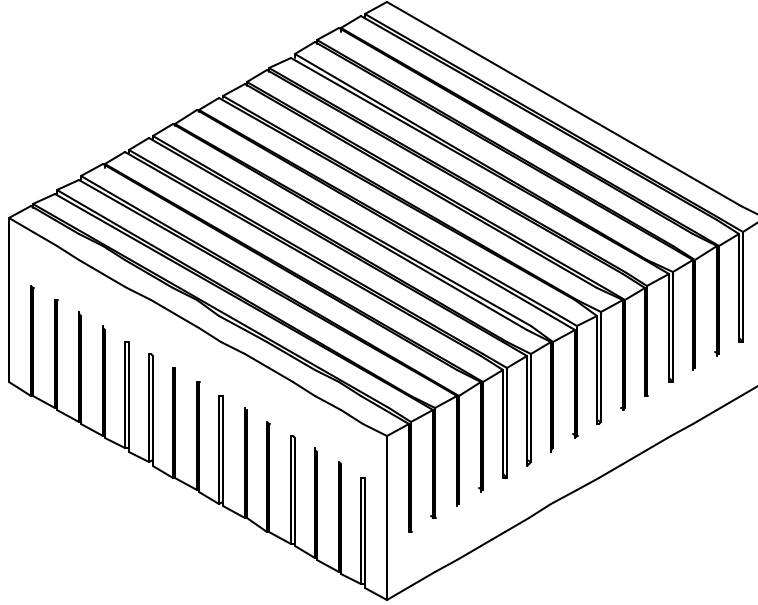
Fig. 4. Fiducial grid plate. The plate is 3" thick, with perpendicular slots 2" deep cut into both faces. Each slot in the top face intersects each slot in the bottom face, forming a regular grid of square holes through the entire block.
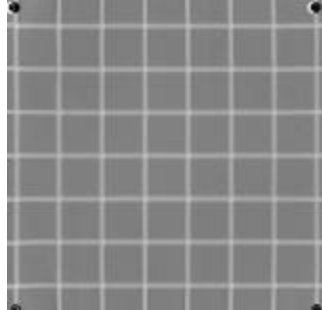
- Divide by beam
- Flatten
- Calibrate using 4 intersections and linear terms only
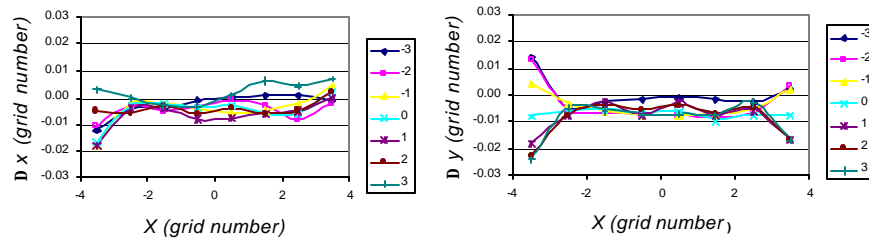- Calibration: 1.427 cm/square

$s_x (cm)$	$s_y (cm)$
0.0072	0.0094

Fig. 5. Radiograph and position residuals from the fiducial plate test.
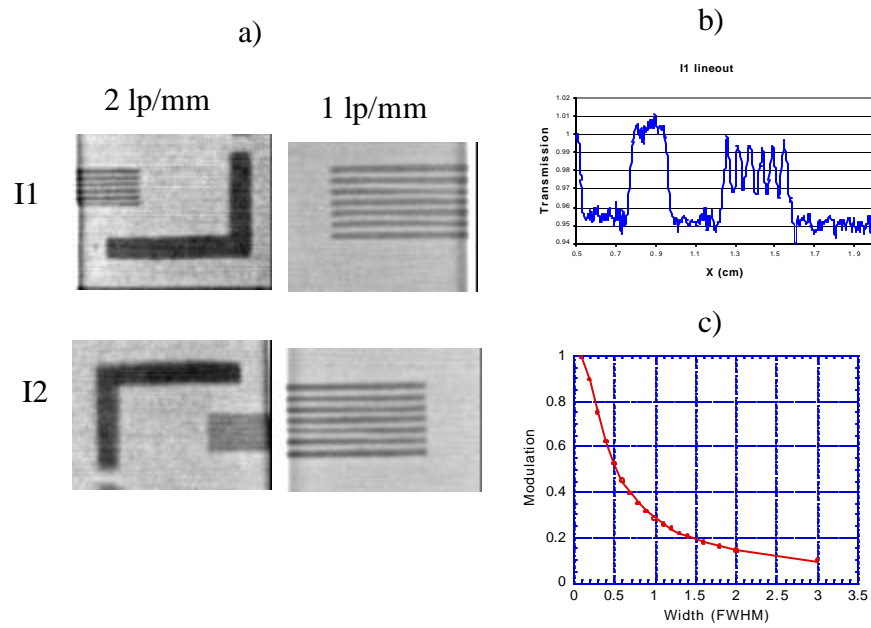
Fig. 6. (a) Radiographs of the resolution test pattern. (b) lineout of the 2 line pair/mm test pattern from image location 1. (c) Plot of the relationship between modulation and resolution.
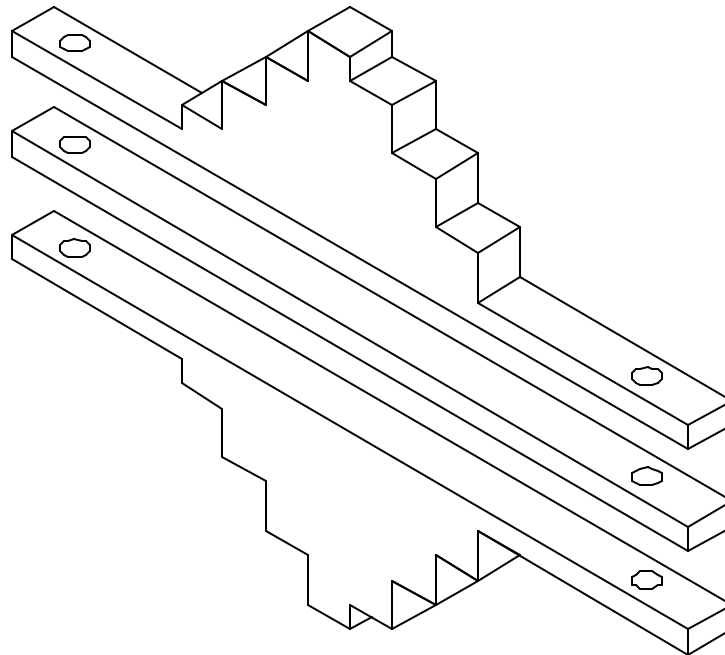

Fig. 7. Doubly symmetrized step wedge. The thickness of the steps decreases on either side of center, more or less following the incident beam intensity. Using a pair of half height wedges back to back keeps the center at a constant position, and allows the insertion of spacer plates of the same material.
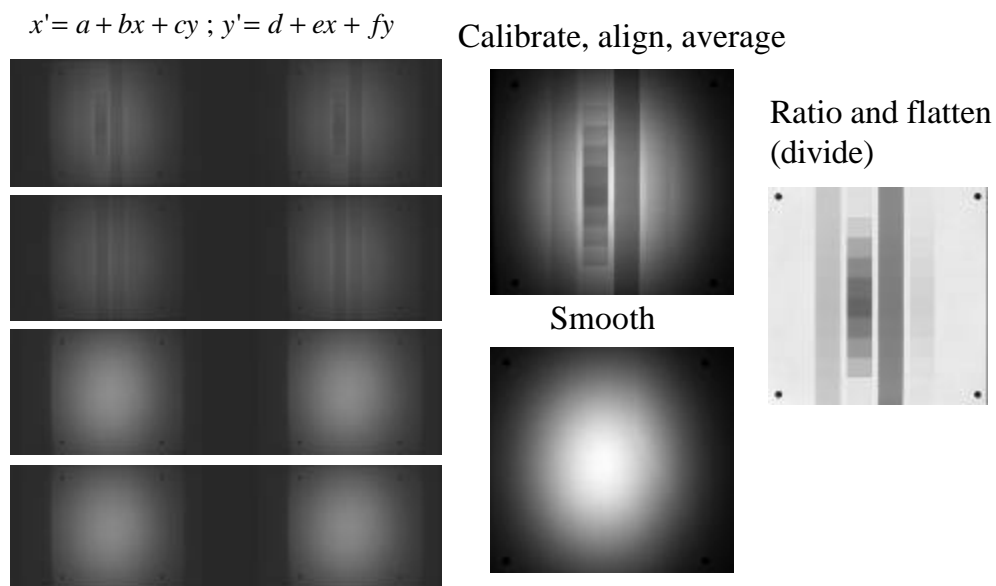
$x' = a + bx + cy$; $y' = d + ex + fy$ Calibrate, align, average

Ratio and flatten
(divide)

Smooth

Fig. 8. Images from the various steps in the analysis procedure.

Tungsten   Carbon

	I	X_0
	(gm/cm^2)	(gm/cm^2)
Copper	124.18	14.47
Carbon	78.70	22.11
Tungsten	173.41	8.38
Lexan	74.01	18.96

Tungsten step wedge

Carbon step wedge

Thickness (gm/cm^2)
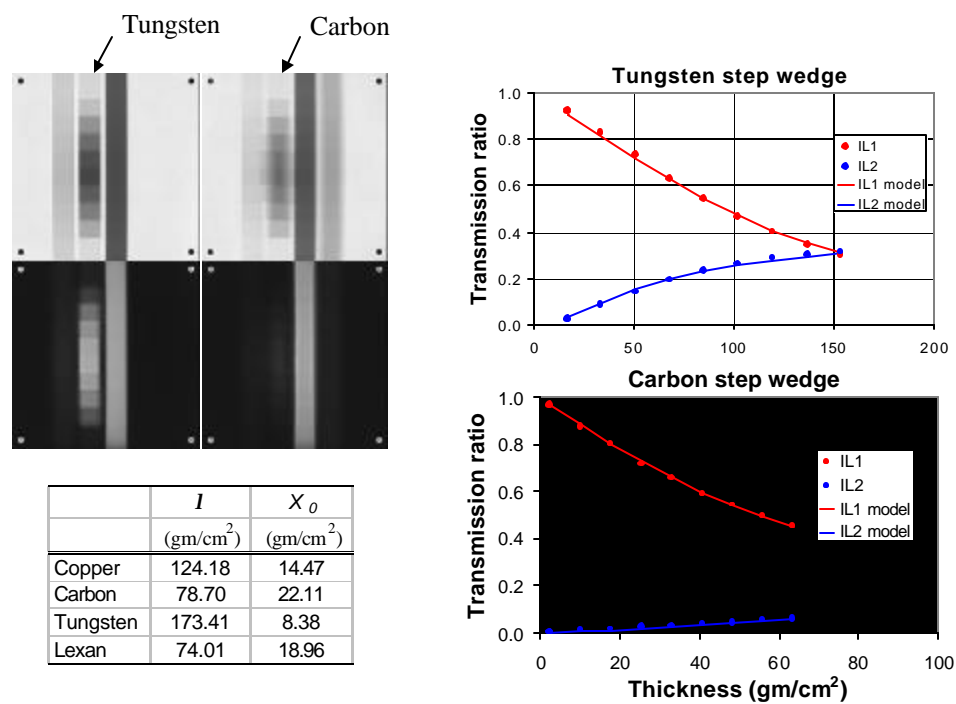
Fig. 9. The carbon and tungsten 10% step wedge data.

Tungsten step wedge fit
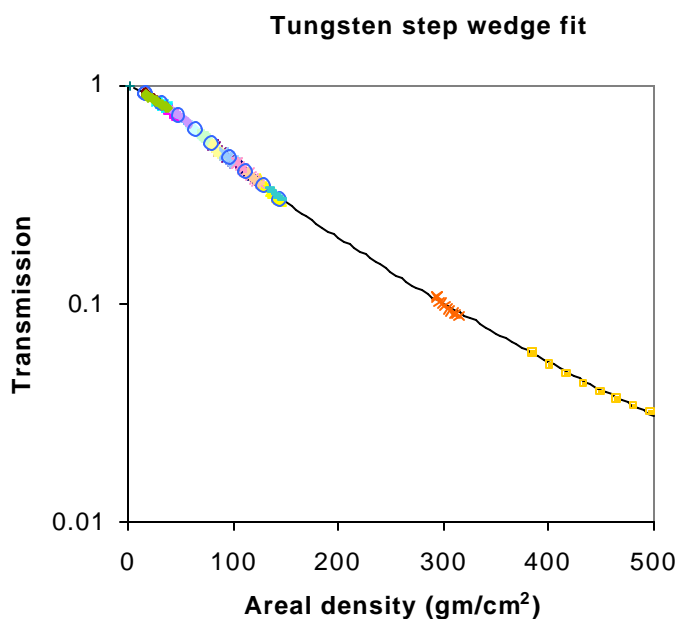
Fig. 10. Image location 1 tungsten step wedge data set. The line is a fit to the data that are used in the FTO analysis.
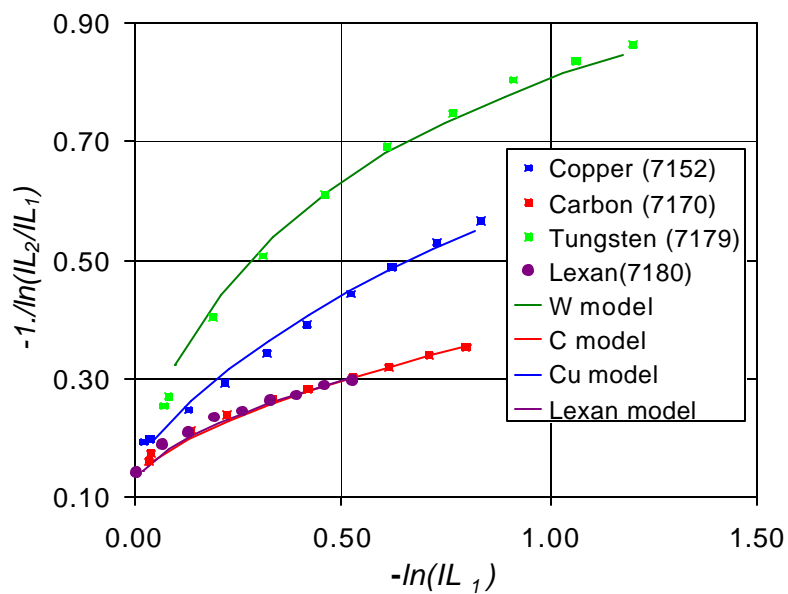

Fig. 11. Plot of the functions of the transmission suggested by Eqs. (10).and (11) to demonstrate material identification. The materials in the step wedges are clearly distinguished by different slopes.

Model of outer shells
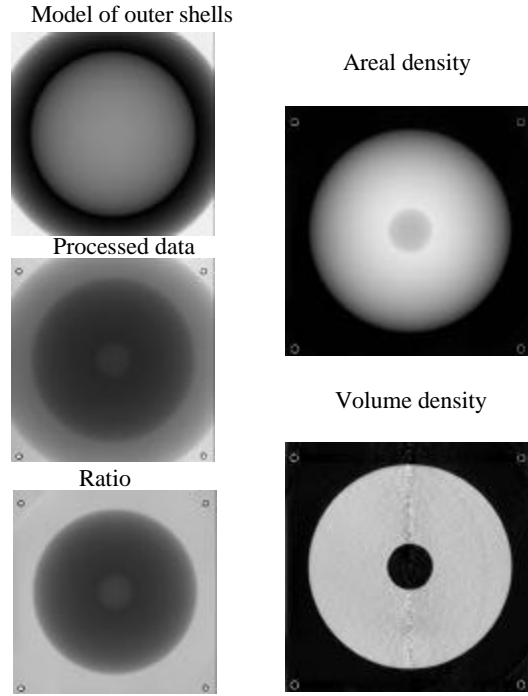

Areal density

Processed data

Volume density

Ratio

Fig. 12. Left top: Model of outer shells; Left middle: Measured transmission data; Left bottom: Measured data divided by the model; Right top: Tungsten areal density; Right bottom: Volume density.

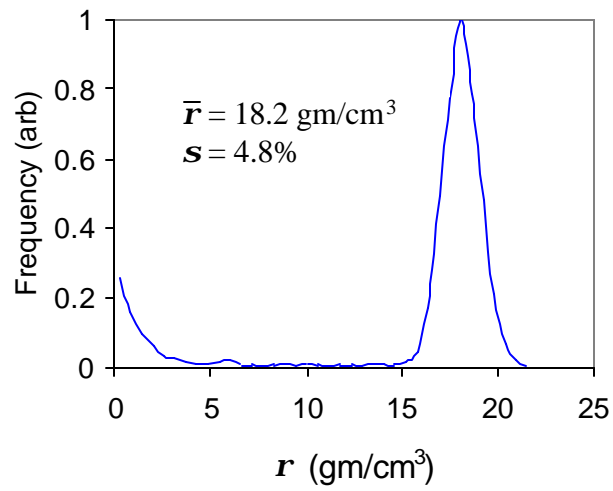$\bar{r} = 18.2 \ \text{gm/cm}^3$
$s = 4.8\%$

Fig. 13. A histogram of radiographically measured densities in the tungsten region of the FTO. The mean value and the width are given in the figure.
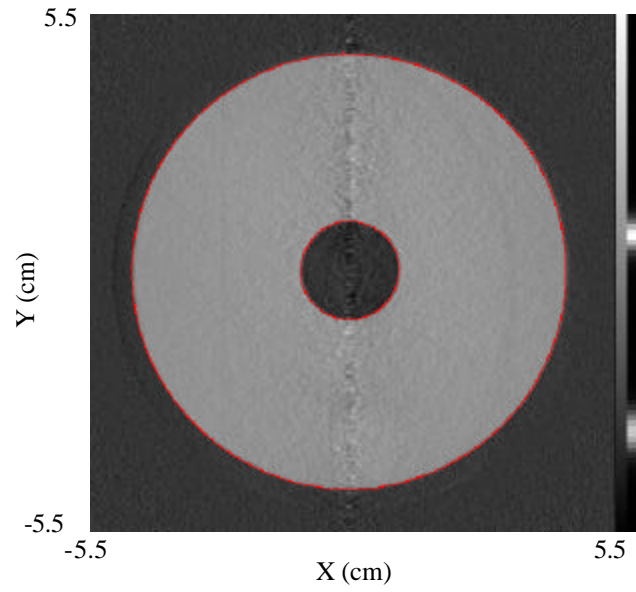
Fig. 14. The red line shows the result of the contour finding routine on the volume density image from the FTO tungsten reconstruction.

$\overline{r_{outer}}$=4.494 cm σ_{outer}=77 μm
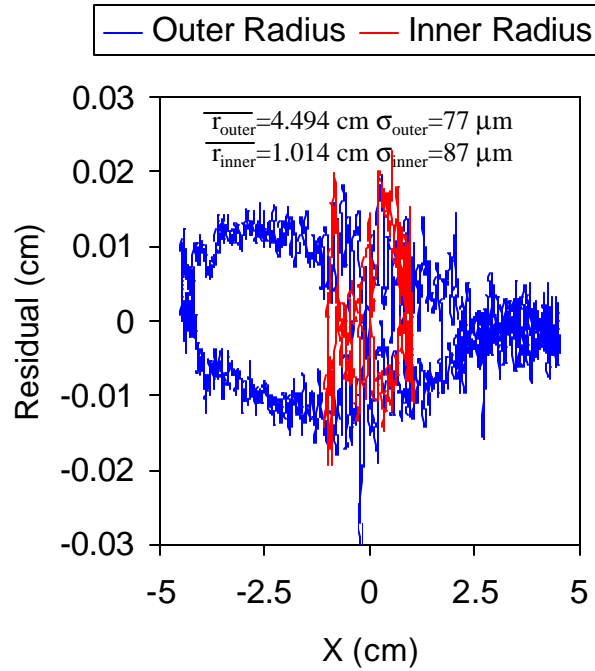$\overline{r_{inner}}$=1.014 cm σ_{inner}=87 μm

Fig. 15. The residual (difference between the radius of the contour and the average radius) for the outer edge of the FTO in blue and the inner edge of the FTO in red.